Nanoscale Research Letters

NANO EXPRESS Open Access

One Step In Situ Loading of CuS Nanoflowers on Anatase TiO_2/Polyvinylidene Fluoride Fibers and Their Enhanced Photocatalytic and Self-Cleaning Performance

Zhi-Guang Zhang[1,2†], Hui Liu[1†], Yu-Qian Cui[3], Min Dong[3], Qing-Hao Li[3], Xiao-Xiong Wang[1], Seeram Ramakrishna[1,4] and Yun-Ze Long[1*]

Abstract

CuS nanoflowers were loaded on anatase TiO_2/polyvinylidene fluoride (PVDF) fibers by hydrothermal treated electrospun tetrabutyl orthotitanate (TBOT)/PVDF fibers at low temperature. The results indicated that the amount of copper source and sulfur source determined the crystallization and morphology of the resultant products. It was found that the composite of CuS narrowed the band gap energy of TiO_2 and enhanced the separation efficiency of the photogenerated electron-hole pairs of TiO_2. The photocatalytic reaction rate of CuS/TiO_2/PVDF fibers to rhodamine B was 3 times higher than that of TiO_2/PVDF fibers under visible light irradiation. Besides, owing to the preparation process was carried out at low temperature, the flexibility of CuS/TiO_2/PVDF fibers was ensured. In addition, the self-cleaning performance of the dye droplets on the resultant product surface was demonstrated under visible light. Meanwhile, the resultant product can automatically remove dust on the surface of the material under the rolling condition of droplets due to its hydrophobicity. Therefore, the as-prepared CuS/TiO_2/PVDF fibers can not only degrade the contaminated compounds, but also depress the maintenance cost owing to its self-cleaning performance, which means a very practical application prospect.

Keywords: CuS, TiO_2, Nanoflower, Fiber, Photocatalysis

Introduction

In recent years, due to the unreasonable development and utilization of natural resources, the environment of human beings has been seriously polluted, including air, soil, and water pollutions. Among them, the water pollution has become one of the urgent problems to be solved because it is closely related to human life. Due to the landmark research of Fujishima and Honda [1], semiconductor photocatalysis technology has won worldwide praise as a potential solution for the degradation of toxic organic pollutants in water to achieve environmental sustainability. So far, many semiconductors have been employed in the water treatment [2–5]. Manikandan et al. synthesized MoS_2/α-MoO_3 heterostructured nanoflowers through one-step hydrothermal method [6]. The as-prepared MoS_2/α-MoO_3 heterostructured nanoflowers have a high surface area and excellent adsorbed performance. Wei and co-workers prepared porous Co_3O_4 nanosheets by hydrothermal method [7]. The resultant products exhibit a much lower overpotential of 318 mV at a current density of 10 mA cm^{-2}. Besides, these porous Co_3O_4 nanosheets also display excellent electrochemical stability. Among many semiconductors, titanium dioxide (TiO_2) has become a well-known photocatalyst because of its unparalleled efficiency and stability. However, the effectiveness of TiO_2 is hindered by its wide band gap (Eg ~ 3.2 eV), which makes

* Correspondence: yunze.long@163.com; yunze.long@qdu.edu.cn
†Zhi-Guang Zhang and Hui Liu contributed equally to this work.
[1]Collaborative Innovation Center for Nanomaterials and Devices, College of Physics, Qingdao University, Qingdao 266071, China
Full list of author information is available at the end of the article

it impossible to directly utilize visible light, leading to the absence of TiO_2 as a visible photocatalyst. In addition, the rapid recombination of photogenerated charge carriers in TiO_2 greatly reduces its light quantum efficiency.

In order to alleviate these problems, a lot of researches have been carried out to enhance the visible light photocatalytic ability of TiO_2 [8–13]. The combination of TiO_2 with other narrow-gap semiconductor components, particularly, two dimensional (2D) narrow-gap semiconductor components, has been proved to be a flourishing strategy in improving the separation efficiency of photoinduced charge carriers [14–21]. Ouyang et al. synthesized BiOCl nanosheets/TiO_2 nanotube arrays heterojunction by the combination of anodization process and impregnation method [22]. The as-prepared products enhanced the separation efficiency of photogenerated charge carriers through the interface between the BiOCl nanosheets and TiO_2 nanotube arrays. In addition, the combination of 2D graphene with good conductivity and TiO_2 can also obtain good photocatalytic performance [23]. Interestingly, research on the complexation with metal sulfides has made some progress [24–29]. Particularly, the TiO_2 samples composited cadmium and lead semiconductor have achieved remarkable performance, but also caused serious secondary pollution problems. Therefore, the exploration of benign narrow band gap semiconductor composites is imperative.

Copper sulfide (CuS), a semiconductor material with a band gap of 2.0 eV, has excellent performance and has been used in solar cells, photocatalysis, lithium batteries, etc. [30, 31]. Therefore, the coupling of CuS and TiO_2 to prepare a CuS-TiO_2 composite with visible light activity and high separation efficiency of photogenerated carriers provides a possibility. Yu and co-workers prepared two different composites TiO_2-CuS-a and TiO_2-CuS-b through direct deposition and bifunctional linker coupling methods on TiO_2 nanospheres [32]. Compared with TiO_2-CuS-a prepared through direct deposition method, TiO_2-CuS-b with a regular "spiky-ball-like" structure has enhanced disinfection ability, which improved its photocatalytic performance under solar and UV light. Lu et al. prepared CuS nanoflowers loaded on rutile TiO_2 using copper and sulfur powder through element-direct-reaction [33]. Compared with pure TiO_2 or copper sulfide, the as-synthesized CuS/TiO_2 samples presented enhanced photocatalytic performance due to the formation of hetero-junction between CuS and rutile TiO_2. Hou et al. prepared TiO_2 fibers by electrospinning and post-sintering. The prepared TiO_2 fibers were soaked in NaOH solution and then grew CuS particles on the surface of the fibers by hydrothermal method [34]. The island-like CuS particles attached to TiO_2 nanofibers which had a diameter less than 100 nm to form heterostructures. The as-prepared samples showed improved photocatalytic activity for the degradation of the methyl blue (MB) dye. The above-mentioned CuS-TiO_2 composites are powdered materials or very brittle fiber materials after high-temperature treatment. These materials are difficult to separate and recycle after photocatalytic experiment in water. In addition, photocatalytic materials often suffer from contamination by target pollutants, resulting in a decrease in their photocatalytic performance.

In this work, CuS nanoflowers were loaded on the TiO_2/polyvinylidene fluoride (PVDF) fibers by one-step hydrothermal treatment on electrospun tetrabutyl orthotitanate (TBOT)/PVDF fibers at low temperature. On the one hand, the preparation process is convenient and simple. On the other hand, the low temperature use in the preparation process guarantees the flexibility of PVDF. The as-prepared CuS/TiO_2/PVDF fiber has good visible light photocatalytic performance. Under visible light, the photocatalytic reaction rate of CuS/TiO_2/PVDF fibers to rhodamine B (RhB) is 3 times higher than that of TiO_2/PVDF fibers. In addition, the self-cleaning performance of the resultant product was investigated. It can be concluded that the as-prepared CuS/TiO_2/PVDF fibers have good separability, recyclability, and self-cleaning performance. The resultant samples in this work provide a new perspective for exploring the application of novel flexible, recyclable, and self-cleaning photocatalytic materials for environmental pollution controllability.

Methods/Experimental

Materials

PVDF (FR904) was purchased from Shanghai 3F New Materials Co., Ltd., and N, N-dimethylformamide (DMF, AR, 99.5%), acetone (CP, 99.0%), TBOT (CP, 98.0%), copper nitrate ($Cu(NO_3)_2{\cdot}3H_2O$, AR, 99.0%), thiourea (AR, 99.0%), RhB, MB, and methyl orange (MO) were purchased from Sinopharm Chemical Reagent Co., Ltd. All reagents were used as received without any further purification.

Preparation of TBOT/PVDF Fibers

In a typical electrospinning process, 4.0 g PVDF powder was mixed with 10 g acetone and 10 g DMF. Then, the mixture was stirred vigorously at 40 °C until it became clear and transparent. After that, 10 ml of TBOT was added to the solution mentioned above and stirred for 1 h at 40 °C to form the TBOT/PVDF precursor solution. A 5.0-ml syringe containing TBOT/PVDF precursor solution with a blunt metal needle was placed on a propeller. The propulsion speed was set at 1.8 ml h^{-1}. The fiber collector was a stainless steel roll wrapped in a piece of aluminum foil with a rotate speed of about 250 rpm. A DC voltage source set to 9 kV was placed between the tip and the collector at a distance of 11 cm. The as-prepared TBOT/PVDF fibers were dried at 60 °C for

10 h to eliminate any remaining solvent. Finally, the as-prepared TBOT/PVDF fibers were cut into 2.5 cm × 2.5 cm pieces for subsequent hydrothermal treatment.

Fabrication of CuS/TiO_2/PVDF Fibers

$Cu(NO_3)_2{\cdot}3H_2O$ and thiourea were added into 30 ml of deionized water in a fixed molar ratio (1:2) and stirring was continued for 30 min. Then, the solution was transferred to the 50-ml stainless steel autoclave, and the cut TBOT/PVDF pieces were placed inside. The stainless steel autoclave was placed in an electric oven and heated at 150 °C for 24 h. In the hydrothermal process, on the one hand, TBOT in TBOT/PVDF is hydrolyzed to form TiO_2/PVDF. On the other hand, CuS is continuously growing on the surface of TiO_2/PVDF to form CuS/TiO_2/PVDF. Finally, the as-prepared fibers were thoroughly washed with ethanol and deionized water, then dried in an electric oven at 60 °C for 10 h and the flexible CuS/TiO_2/PVDF fibers were obtained (shown in Additional file 1: Figure S1. For comparison, the amount of $Cu(NO_3)_2{\cdot}3H_2O$ added was 0.1, 0.5, and 1 mmol, respectively. Correspondingly, the as-synthesized materials were named as Cu 0.1, Cu 0.5, and Cu 1, respectively.

Characterization

The X-ray diffraction (XRD) patterns were carried out on a Rigaku SmartLab X-ray diffractometer in the 2θ range of 10–90° using Cu-Kα radiation (λ = 1.54178 Å) at an accelerating voltage of 40 kV. In addition, the scanning electron microscopy (SEM) images and transmission

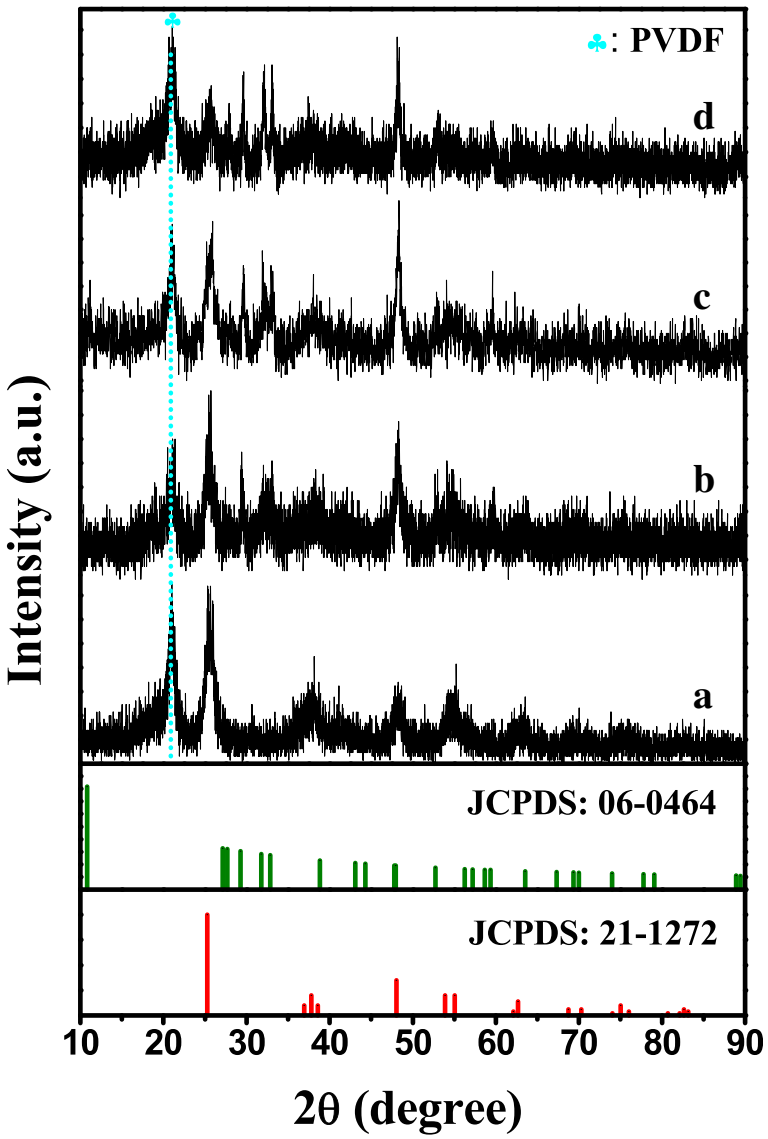

Fig. 1 XRD patterns of (a) TiO_2/PVDF fibers, (b) Cu 0.1, (c) Cu 0.5, and (d) Cu 1

electron microscopy (TEM) images of the as-prepared samples were obtained from Phenom Pro scanning electron microscope and JEOL JEM-2100 Plus transmission electron microscope, respectively. To achieve a detailed understanding of the chemical composition information of the as-prepared products, the X-ray photoelectron spectroscopy (XPS) detections were operated on a Thermo Scientific Escalab 250Xi system. The light-harvesting performance of the as-prepared samples was evaluated by diffuse reflectance spectra (DRS). DRS investigations were carried out on Shimadzu UV-2600 spectrophotometer equipped with an integrating sphere accessory and using $BaSO_4$ as a diffuse reflectance standard. The photoluminescence spectra (PL) of the resultant samples were studied on a Hitachi F-2500 fluorescence spectrometer with a Xe lamp at room temperature using an excitation wavelength of 320 nm.

Photocatalytic Activity

The photocatalytic performances of the resultant products were investigated under a 9-W white light LED irradiation at room temperature by degrading RhB ($5\ mg\ L^{-1}$) which was directly prepared with RhB reagent and deionized water. The light spectrum of this LED is shown in Additional file 1: Figure S2. In order to show the effect of the amount of Cu sources on photocatalysis, the film photocatalysts with the same area were used in photocatalysis experiments. In photodegradation experiments, a piece of the resultant product was put into a 100-ml quartz tube with 60 ml RhB solution followed by 30-min magnetic stirring in the dark to ensure the adsorption-desorption equilibrium between RhB and the resultant product. Then, the quartz tube was placed under the light source with a distance of 4.0 cm. At given time intervals, 3 ml solution was taken out from the quartz tube followed by centrifuging to remove the particles. Then, the concentration of RhB remained in the solution was investigated its absorbance at 554 nm on a Shimadzu UV-2600 spectrophotometer. In order to ensure a roughly equivalent volume of solution, the analyzed solution was quickly poured back into the quartz tube after every assay.

The ratio of RhB concentration C at each interval to the initial concentration C_0 was used to indicate the

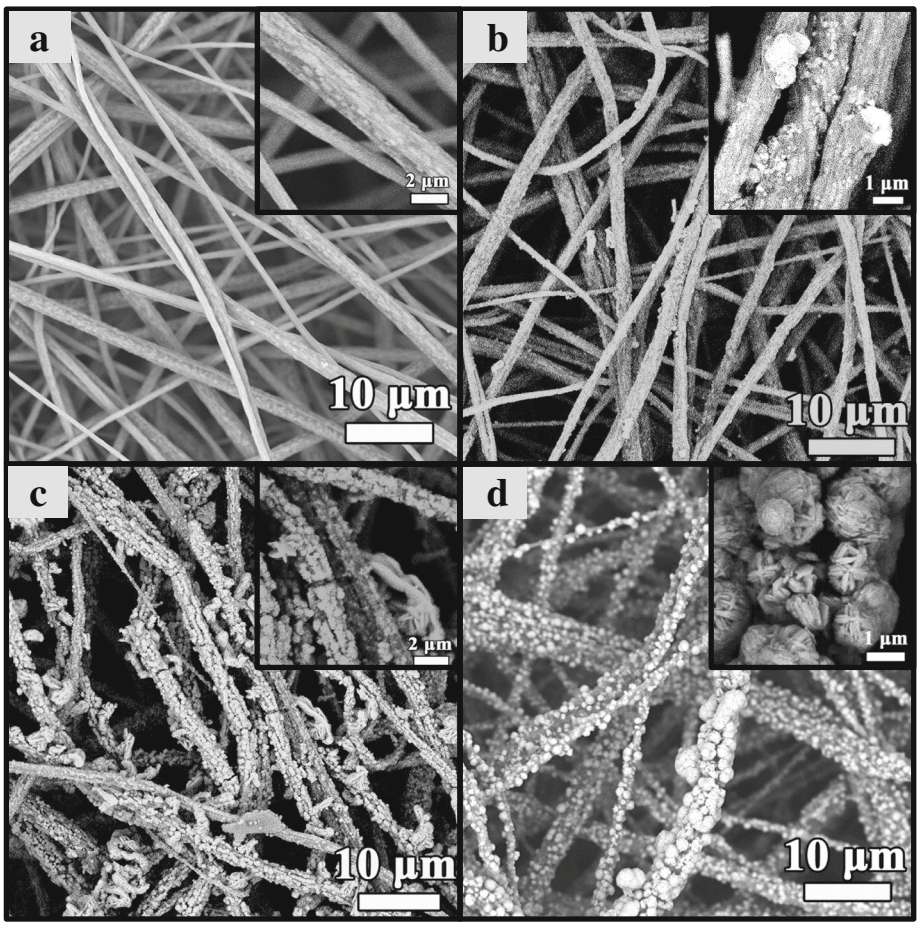

Fig. 2 SEM images of **a** TiO_2/PVDF fibers, **b** Cu 0.1, **c** Cu 0.5, and **d** Cu 1

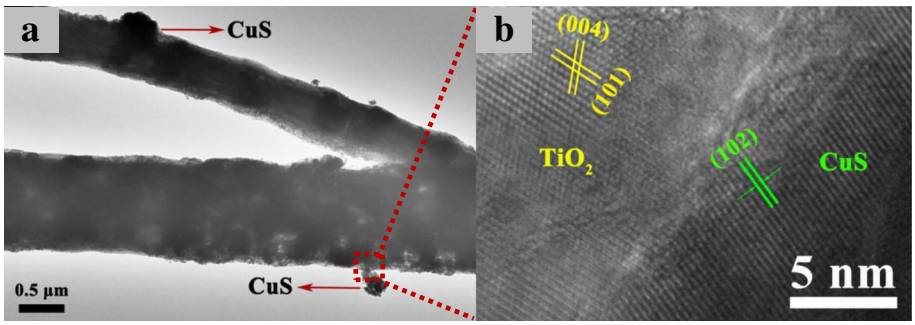

Fig. 3 TEM image of Cu 1 **a** and high-resolution TEM image of Cu 1 **b**

photocatalytic degradation efficiency, which was expressed as C/C_0. After the photocatalytic degradation experiment, the resultant product was washed with ethyl alcohol and deionized water followed by drying in air for the next photodegradation process to study the recycle stability performance of the resultant product.

Self-Cleaning Performance

Wetting Property

The wetting property of CuS/TiO_2/PVDF fibers is obtained by testing the contact angle of the droplets (including H_2O, RhB, MO, and MB) on the product under ambient temperature through a Theta Attension optical contact angle instrument.

Self-Cleaning Performance

Self-cleaning performance of the resultant product is evaluated by degrading surface dye droplets and removing surface dust. The RhB, MO, and MB dye droplets with a concentration of 10 mg L^{-1}were dripped onto the CuS/TiO_2/PVDF fibers and irradiated under the 9-W white lights LED. At given time intervals, an optical photograph was taken, which was used to study the self-cleaning performance of the as-prepared product to the surface contamination. For the surface dust removal of the CuS/TiO_2/PVDF fibers, the dust was scattered on the surface of the sample before measurement. Then, a drop of water was dropped on the surface of the product. The sample was tilted slightly to make the droplet

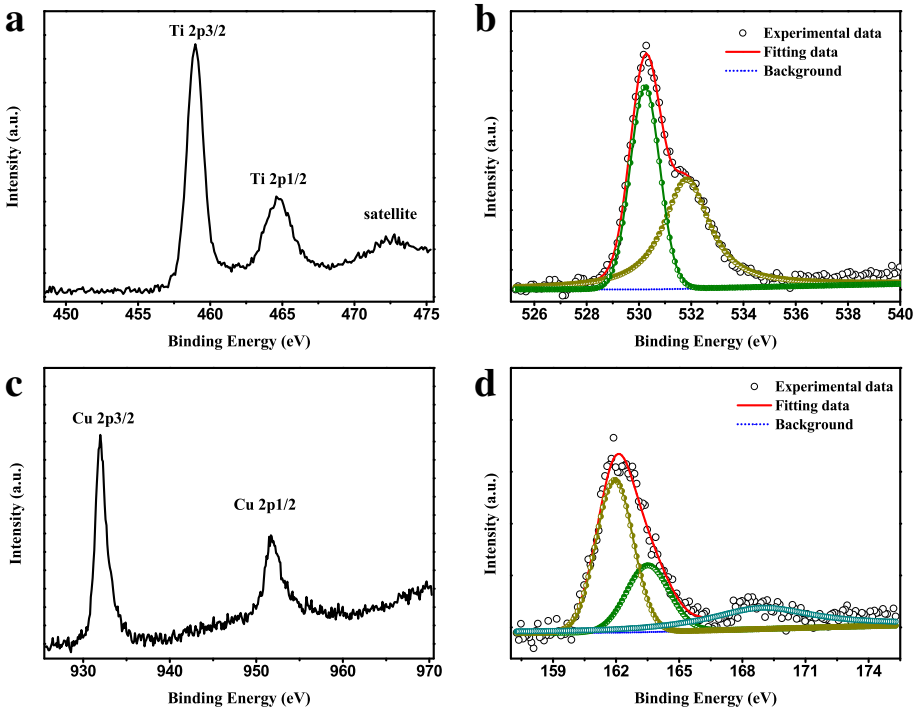

Fig. 4 High-resolution XPS spectra of **a** Ti 2p, **b** O 1s, **c** Cu 2p, and **d** S 2p in Cu 1 sample

Table 1 The atomic concentration of element in Cu 1 sample

Element	C	F	Ti	O	Cu	S
Atomic concentration	50.08	28.81	4.01	11.58	2.43	3.09

move on the sample surface and take away the dust, thus making the material surface clean.

Results and Discussion

Structure and Morphology Characteristics

The XRD patterns of TiO_2/PVDF fibers, Cu 0.1, Cu 0.5, and Cu 1 are depicted in Fig. 1. It is evident that no obvious diffraction peak is detected except the diffraction peak of PVDF and TiO_2 as displayed in Fig. 1 curve a. The diffraction peak around 20.8° can be assigned to the β phase of PVDF, and the diffraction peak at 25.67°, 37.8°, 48.2°, and 54.6° can be assigned to the (101), (004), (200), and (211) crystal faces of anatase phase TiO_2 (PDF card 21-1272, JCPDS), respectively [35–37]. Comparing curve b with curve a, there are two obvious diffraction peaks near the diffraction angles of 29.4° and 32.6° in curve b, which can be indexed to the (102) and (006) crystal faces of hexagonal CuS (PDF card 06-0464, JCPDS). In addition, it is worth noting that the diffraction peak near 48.3 in curve b is stronger than that in curve a, which mainly due to the fact that the diffraction peaks of TiO_2 and CuS are superimposed at this diffraction angle. These indicate that the CuS is successfully formed on the TiO_2/PVDF fibers. Furthermore, a diffraction peak appears gradually near the diffraction angle 27.7° in curve c and d compared with curve b, which corresponds to (101) crystal faces of CuS. Meanwhile, the diffraction peak near 32.6° also gradually become two distinct peaks at 31.9° and 32.9°, respectively, corresponding to (103) and (006) crystal faces of CuS. Based on the results mentioned above, it can be found that with the increase of Cu and S sources, the crystallization of CuS becomes better.

The typical SEM images of TiO_2/PVDF fibers, Cu 0.1, Cu 0.5, and Cu 1 are displayed in Fig. 2. As can be seen from Fig. 2a, the TiO_2/PVDF fibers are arranged in disorder with a relatively rough surface (displayed in the inset) which mainly due to the formation of TiO_2 in the fibers. Comparing Fig. 2b with Fig. 2a, the surface of fibers in Fig. 2b becomes rougher, and a small amount of CuS particles have appeared on the surface of fibers which can be easily found in the inset illustration. When the amount of Cu source increases to 0.5 mmol, a very large change can be found in comparison with Fig. 2b that a large amount of CuS particles coat on the surface of TiO_2/PVDF fibers, as shown in Fig. 2c. Furthermore, it can be seen from the inset illustration that a small amount of hexagonal layered CuS nanoflowers appears on the surface of TiO_2/PVDF fibers. When the amount of Cu source increase to 1 mmol, obviously, a large number of aggregated CuS particles have appeared on the fiber surface (depicted in Fig. 2d). Through careful examination of the inset of Fig. 2d, these large CuS nanoflowers are composed of many hexagonal lamellar CuS. Based on the above results, it can be known that the increase of Cu source, on the one hand, continuously increases the amount of CuS on the surface of the fiber and, on the other hand, enhances the crystallization and growth of CuS on the surface of the fiber leading to the

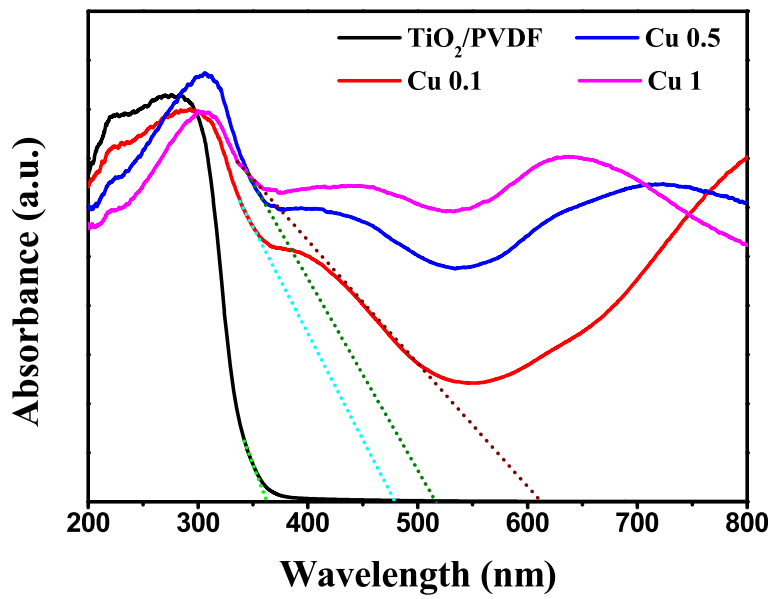

Fig. 5 UV-Vis diffuses reflectance spectra of TiO_2/PVDF, Cu 0.1, Cu 0.5, and Cu 1

Table 2 Absorption edge and energy band gap of TiO_2/PVDF, Cu 0.1, Cu 0.5, and Cu 1 samples

Typical sample	Absorption edge (nm)	Energy band gap (eV)
TiO_2/PVDF	363	3.4
Cu 0.1	479	2.6
Cu 0.5	517	2.4
Cu 1	612	2.0

morphology of CuS gradual change from particles to hexagonal lamellar structure.

The morphology of CuS/TiO_2/PVDF fiber is further investigated by TEM and HRTEM, as presented in Fig. 3. As depicted in Fig. 3a, it is evident that some CuS particles with uneven size are distributed on the surface of TiO_2/PVDF fiber. The contact position between CuS and TiO_2/PVDF fiber is enlarged to obtain a high-resolution image, as shown in Fig. 3b. From the high-resolution TEM image, it can be found that CuS and TiO_2 have obvious crystal boundary. By measuring the interplanar spacing, it can be found that there are mainly two kinds of crystal faces of TiO_2 with the interplanar spacing of 0.35 and 0.23 nm, respectively, corresponding to the (101) and (004) crystal faces of TiO_2. The angle between these two crystal faces is about 68°, which is consistent with the literature [38]. In addition, there is mainly a crystal face with a crystal interplanar spacing of about 0.31 nm, corresponding to the (102) crystal face of CuS. Therefore, the TEM and HRTEM studies are consistent with the XRD measurements.

XPS analysis is employed to study the chemical composition information and the bonding configuration of the resultant products. Characteristic peaks of Cu, S, Ti, O, F, and C can be clearly detected from the XPS survey spectra, as shown in Additional file 1: Figure S3. The high-resolution XPS spectra of Ti 2p, O 1s, Cu 2p, and S 2p are illustrated in Fig. 4. As can be seen in Fig. 4a, the peaks located at 459.0 and 464.7 eV can be assigned to Ti $2p_{3/2}$ and Ti $2p_{1/2}$, respectively [39]. The peak of O1s can be divided into two peaks (displayed in Fig. 4b), respectively, corresponding to Ti-O of TiO_2 (530.2 eV) and hydroxyl group (531.8 eV) in the as-prepared product [40, 41]. In Cu 2p profiles (Fig. 4c), the peaks located at 932.0 and 952.0 eV are indexed to $2p_{3/2}$ and $2p_{1/2}$ of Cu^{2+}, respectively [42]. Meanwhile, for the peaks of S element (depicted in Fig. 4d), the broad spectra located around 162.1 eV can be broken into two peaks of 161.9 and 163.5 eV, respectively, corresponding to the $2p_{3/2}$ and $2p_{1/2}$ of S^{2-} [43]. In addition, a weak peak at 168.8 eV is detected which may be the intermediate products produced by thiourea in hydrothermal reaction [44]. Furthermore, the atomic concentration from high-resolution XPS spectra is depicted in Table 1. It is easy to find that the ratio of O to Ti atoms is more than 2:1, which is mainly due to the presence of O atoms in PVDF [45]. The ratio of S to Cu atoms is about 1.27, which is a little more than 1:1. The main reason is that the excessive S source (the ratio of Cu source to S source is 1:2) is used in the preparation process, resulting in some S remaining on the surface of the sample. The XPS results mentioned above further confirm the

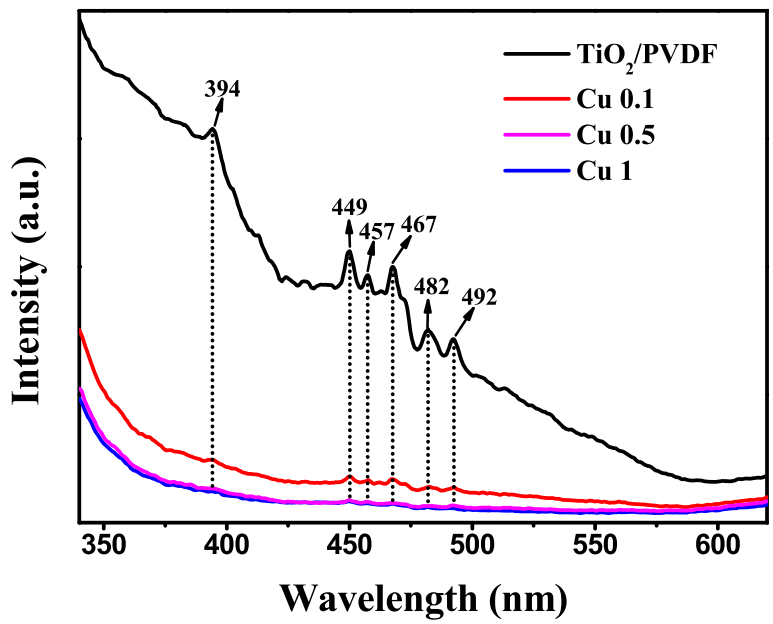

Fig. 6 PL spectra of TiO_2/PVDF, Cu 0.1, Cu 0.5, and Cu 1

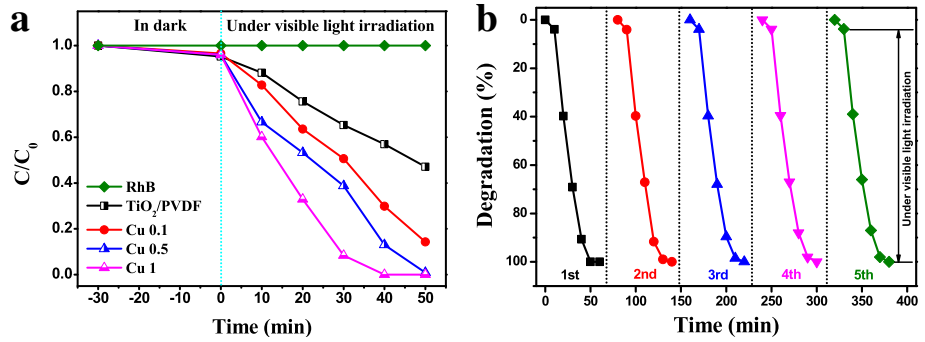

Fig. 7 **a** Photocatalytic degradation curves of RhB over the samples: RhB without photocatalyst, TiO_2/PVDF, Cu 0.1, Cu 0.5, and Cu 1. **b** The recycle experiment using the sample Cu 1

presence of CuS, TiO_2, and PVDF in the Cu 1 sample, which agree well with the XRD and TEM results.

Optical Characteristics

The optical characteristics of TiO_2/PVDF, Cu 0.1, Cu 0.5, and Cu 1 are studied by UV-Vis diffuse reflectance spectra which are transformed to absorbance values using the Kubelka-Munk function [35, 46], as illustrated in Fig. 5. It is easy to find that the absorbance value of the samples composited CuS is much higher than that of TiO_2/PVDF fibers in the visible light region, implying that the composite of CuS greatly enhances the light harvest performance of TiO_2. Furthermore, the absorbance value of samples composited CuS increases continuously with the increase of the amount of Cu source.

According to the previous literature, anatase TiO_2 belongs to indirect band gap semiconductor, while CuS belongs to direct band gap semiconductor [47, 48]. Their energy band gap (Eg) is measured by equation $Eg = 1240/\lambda_g$ (eV), where λ_g is the absorption edge calculated from the intercept between the tangent of the absorption curve and the abscissa coordinate [49]. The absorption edge and energy band gap of the resultant samples are depicted in Table 2.

As can be seen from Table 2, the energy band gap of CuS/TiO_2/PVDF fiber is smaller than that in TiO_2/PVDF fiber, and the absorption edge of CuS/TiO_2/PVDF fiber shifts to the long wavelength gradually with the increase in the amount of Cu source. It is possible that with the increase in the amount of Cu source, CuS is more and more tightly wrapped on the surface of TiO_2/PVDF fiber (as depicted in SEM images), which makes the interface contact between TiO_2 and CuS become larger, resulting in the absorption edge of TiO_2 moving to a long wavelength [50]. Besides, with the increase of Cu source, the crystalline of CuS becomes better which reduces the energy band gap of the resultant product [51, 52].

The PL spectra are usually employed to investigate the recombination of photo-generated electron-hole pairs in the semiconductor [53, 54]. The PL spectra of TiO_2/PVDF, Cu 0.1, Cu 0.5, and Cu 1 samples are displayed in Fig. 6. It can be found in Fig. 6 that there is an emission peak around 394 nm (~ 3.2 eV) in the TiO_2/PVDF fiber and Cu 0.1 also has a weak emission peak here. The position of this emission peak is close to the band-edge emission of TiO_2 in these two samples and should be the near-band-edge emission of TiO_2 [55, 56]. In Cu 0.5 and Cu 1 samples, these emission peaks disappear. In addition, there are five emission peaks in the TiO_2/PVDF fiber between 449 nm (2.76 eV) and 492 nm (2.52 eV), which should be caused by oxygen vacancy (V_O) defects

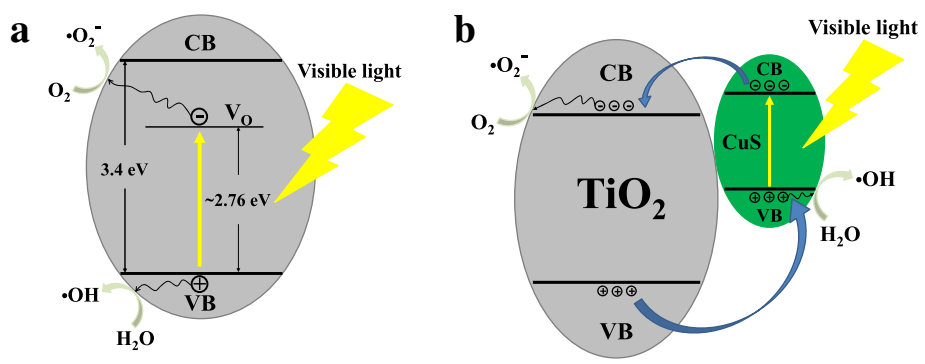

Fig. 8 Diagram of the separation and transmission process of photogenerated electron-hole in **a** TiO_2/PVDF fiber and **b** CuS/TiO_2/PVDF fiber

generated during the preparation process [57, 58]. In the samples of Cu 0.1, Cu 0.5, and Cu 1, these five emission peaks still exist, while the intensity of these five emissions sharply declines, mainly due to the CuS covers on the surface of the TiO_2/PVDF fiber and weakens the intensity of the emission peak.

Besides, the intensity of the PL spectra of the CuS/TiO_2/PVDF fibers is much lower than that of the TiO_2/PVDF fiber, proving that the composite of CuS increases the separation efficiency of photogenerated electron-hole pairs and suppresses the recombination of photogenerated electron-hole pairs, which also means that photocatalytic ability of TiO_2/PVDF fiber is enhanced.

Photocatalytic Performances

The photocatalytic performances of the as-prepared samples are depicted in Fig. 7. It can be seen in Fig. 7a that the concentration of RhB does not change under visible light, which meant that it was very stable under visible light without spontaneous degradation. However, it is interesting to note that TiO_2/PVDF fiber should have only ultraviolet photocatalytic ability but has visible light photocatalytic ability, and its photodegradation of RhB reached 52.9% in 50 min. Compared with TiO_2/PVDF fiber, the Cu 0.1 and Cu 0.5 samples have a faster photocatalytic rate, and the photocatalytic efficiencies of RhB in 50 min are 85.7% and 99.2%, respectively. As can be seen from Fig. 7a, the Cu 1 sample has the highest photodegradation rate, which degrades RhB completely in 40 min.

In addition, the photocatalytic degradation of RhB can also be represented by a pseudo-first-order kinetics process. The equation is as follows [59]:

$$-\ln(C/C_0) = kt$$

where k and t are the reaction rate constant and measurement time, respectively; C_0 and C are the concentration of RhB at initial and t time. According to the equation, the reaction rate constant of RhB degradation by the as-prepared photocatalyst is calculated, as shown in Additional file 1: Figure S4. It can be seen that the reaction rate constant of Cu1, Cu0.5, Cu0.1, and TiO_2/PVDF is 2.9×10^{-2}, 1.8×10^{-2}, 1.6×10^{-2}, and 9.8×10^{-3} min^{-1}, respectively. It is obvious that the reaction rate of Cu1 is about 3 times higher than that of TiO_2/PVDF.

The photocatalytic recycle experiments are carried out on the Cu1 sample for 5 times, as displayed in Fig. 7b. It can be seen that the photocatalytic efficiency of Cu1 sample decreases slightly at 40 min, but remains 100% at 50 min, implying the as-prepared product has a certain recycled stability.

Usually, the photo-induced holes (h^+), superoxide anion radicals ($O_2^{\cdot-}$), and hydroxyl radicals (OH·) are considered as the main active species in the photocatalytic process. [60] Here, in order to investigate the photocatalytic mechanism of the TiO_2/PVDF and CuS/TiO_2/PVDF fibers, control experiments are carried out using ethylenediaminetetraacetic acid (EDTA), nitrogen (N_2), and tertiary butanol (tBuOH) as the individual

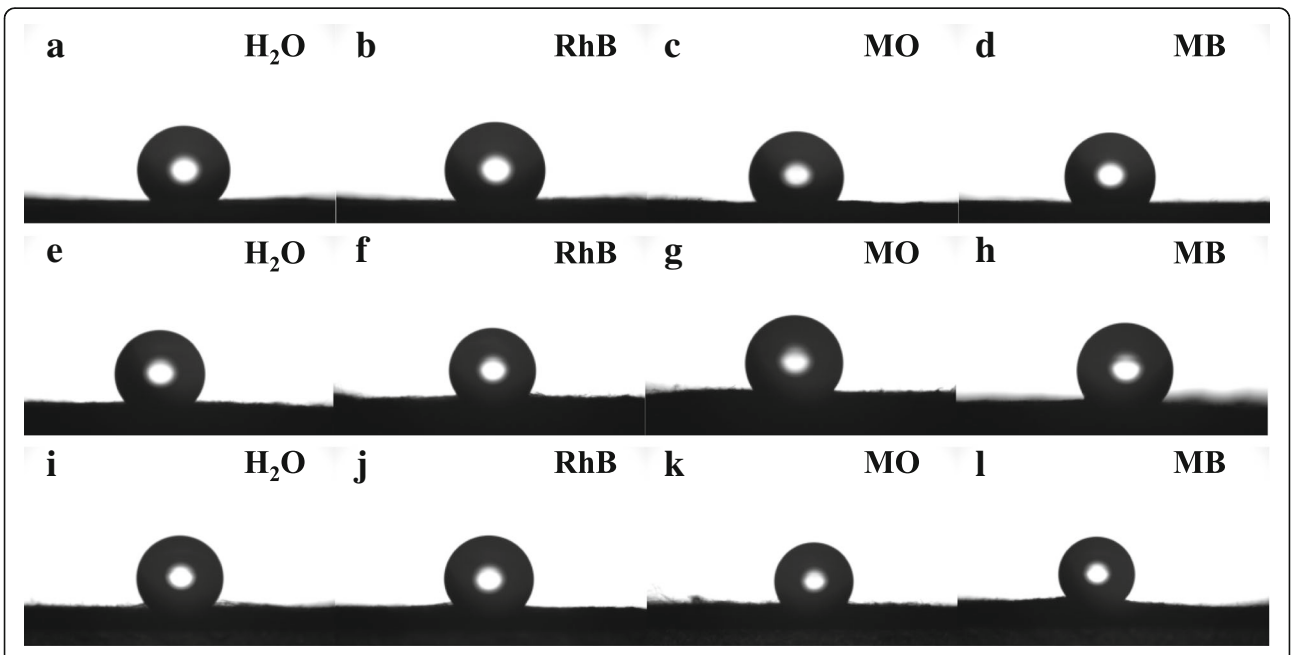

Fig. 9 The optical images of static contact angle for **a**–**d** TiO_2/PVDF fibers, **e**–**h** Cu 0.1, and **i**–**l** Cu 1

Table 3 The static contact angle of TiO_2/PVDF fibers, Cu 0.1, and Cu1

Typical sample	H_2O	RhB	MO	MB
TiO_2/PVDF	135.63 ± 0.16	125.89 ± 0.86	126.30 ± 0.91	126.84 ± 0.18
Cu 0.1	127.10 ± 0.78	125.98 ± 0.91	124.74 ± 0.84	123.70 ± 0.69
Cu 1	125.68 ± 0.12	125.90 ± 0.48	124.25 ± 0.45	125.13 ± 0.51

scavengers for h^+, $O_2^{-\cdot}$, and OH·, respectively, as displayed in Additional file 1: Figure S5. It can be seen that $O_2^{-\cdot}$ have the greatest influence on photocatalytic efficiency in the TiO_2/PVDF system, followed by h^+ and OH·. Whereas in the CuS/TiO_2/PVDF system, h^+ have the greatest influence on photocatalytic efficiency followed by OH· and $O_2^{-\cdot}$.

A possible mechanism is proposed to be responsible for the photocatalytic mechanisms of the TiO_2/PVDF fiber and CuS/TiO_2/PVDF fiber under visible light irradiation as depicted in Fig. 8. For the TiO_2/PVDF fiber, there are a large number of oxygen vacancy defects (V_O) in TiO_2/PVDF fiber, which can be confirmed in the PL spectra. These oxygen vacancy defect levels lie between the valence band (VB) and conduction band (CB) of TiO_2. When irradiated under visible light, the electrons are excited from the VB of TiO_2 and trapped by these defects, leaving a hole in the VB of TiO_2. A part of the photogenerated electrons and holes migrate to the surface of TiO_2 and react with oxygen molecules in the solution to form $O_2^{-\cdot}$ or react with water molecules to form OH·, thereby degrading RhB.

Since the narrow band gap CuS is coated on the surface of the TiO_2/PVDF fiber, the CuS absorbs visible light so that electrons on the VB of CuS are excited to its CB, leaving holes in the VB. Owing to the CB energy of TiO_2 is lower than that of CuS, electrons will be transferred from the CB of CuS to the CB of TiO_2, and holes will be transferred from the VB of TiO_2 to the VB of CuS [40]. The electrons transferred to the CB of TiO_2 react with the oxygen molecules in the solution to form $O_2^{-\cdot}$. And the holes that migrate to the VB of CuS react with the water molecules in the solution to form OH·, thereby degrading RhB.

The composite CuS to the TiO_2/PVDF fiber narrows the band gap of the material and enlarges the absorption range of light on the one hand. On the other hand, the ability of the material to separate photogenerated electron holes is improved, implying the photocatalytic ability is enhanced.

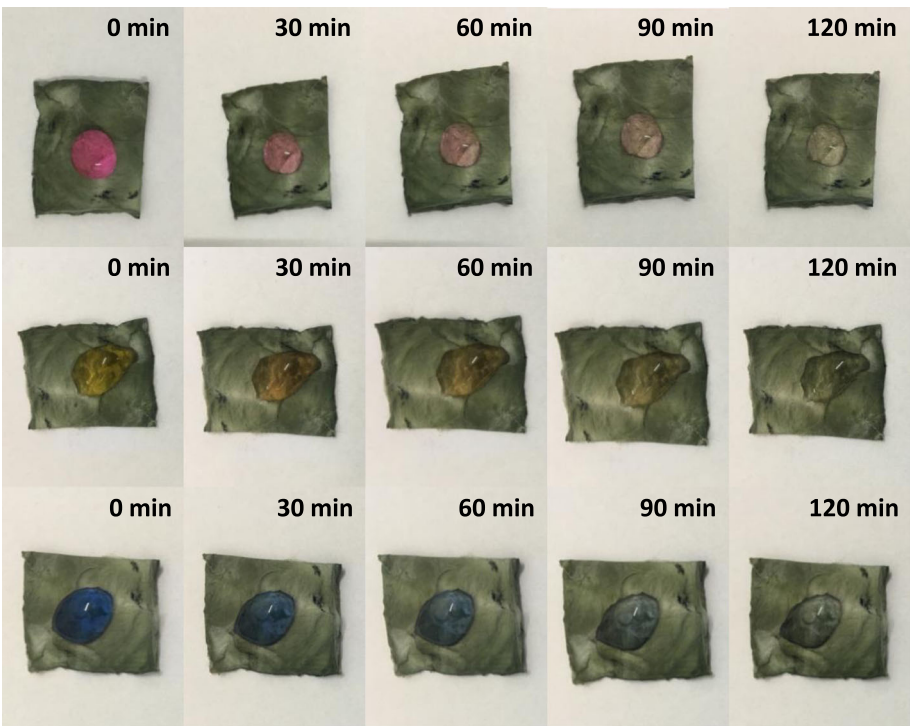

Fig. 10 The optical photograph of the RhB, MO, and MB droplet on the surface of Cu 1 under visible light illumination

Self-Cleaning Performances

The wetting property of the surface decides the self-cleaning mechanism. The static contact angle, which is the contact angle between solid and liquid, is a main parameter to study the surface wetting behavior. The contact angles of H_2O, RhB, MO, and MB for TiO_2/PVDF fibers, Cu 0.1, and Cu 1 are shown in Fig. 9 and Table 3. It can be found that the three samples all show hydrophobicity. However, compared with TiO_2/PVDF fibers, the hydrophobicity of Cu 0.1 and Cu 1 decreased slightly.

In addition, the self-cleaning properties of Cu 1 were investigated by dropping 10 mg L^{-1} of RhB, MO, and MB onto the surface of the resulted product under visible light illumination, as presented in Fig. 10. It is obviously that the colors of these dyes almost disappear in about 120 min, leaving only transparent droplets on the surface of the material. As we know, in the photocatalysis process, the photocatalysts are easily attached to dye molecules causing self-pollution, which reduces its photocatalytic performance. The as-prepared products can greatly improve the photocatalytic effect in practical use due to their self-cleaning ability.

Furthermore, due to the hydrophobicity of Cu 1 surface, water droplets can remain on the product surface. Therefore, the dust can be cleaned from the sample surface through rolling the water droplets on the surface to obtain self-cleaning effect. As displayed in Fig. 11a, before dropping water onto the surface of the sample, the sample presented a clean green surface. To show the self-cleaning effect, a layer of dust was scattered on the sample surface. Following it, a water droplet was dropped onto the surface of the sample. Slightly tilted the sample, the water droplet rolls on sample surface and brings dust down to present the original green surface. This means that in actual use, the prepared product can remove the attached dye or dust by sunlight or rain, thereby reducing maintenance costs.

Conclusions

CuS nanoflowers were loaded TiO_2/PVDF fibers through one-step hydrothermal method on electrospun TBOT/PVDF fibers. The method is very simple and convenient. In addition, the CuS/TiO_2/PVDF fibers were prepared at lower temperature to ensure its flexibility. In the preparation process, the amount of Cu source determines the amount and crystalline quality of CuS supported on TiO_2/PVDF fibers. When the amount of the Cu source reaches 1 mmol, the CuS supported on TiO_2/PVDF fibers was a nanoflower-like structure formed by a hexagonal layer. The composite of CuS narrows the band gap energy of TiO_2 and enhances the light harvest capability of TiO_2. Besides, the composite of CuS increases the separation efficiency of the photogenerated electron-hole pairs of TiO_2, correspondingly, improving

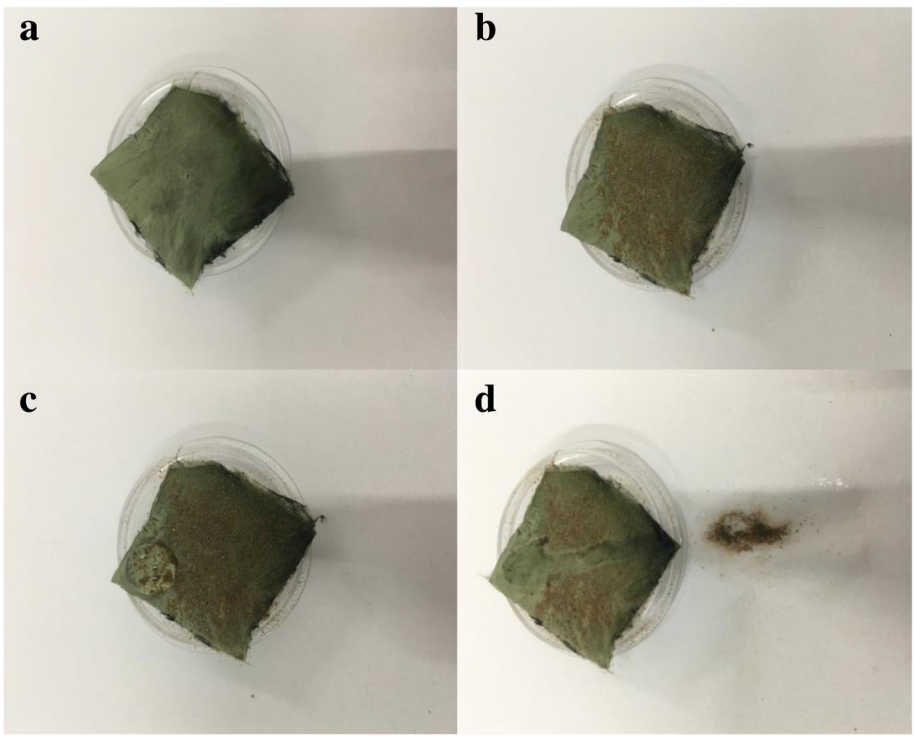

Fig. 11 The optical photograph of a water drop rolling on the surface of Cu 1 to remove dust: **a** clean sample, **b** sample with dusty surface, **c** drop droplets on dust-covered samples, and **d** the droplets roll away the dust and expose the clean surface of the sample

the photocatalytic ability of TiO_2 under visible light irradiation. The photocatalytic reaction rate of CuS/TiO_2/PVDF fibers to RhB is 3 times higher than that of TiO_2/PVDF fibers under visible light irradiation. In addition, after 5 times of recycle, the photocatalytic properties of CuS/TiO_2/PVDF fibers did not decrease which mainly due to its flexibility and reusability. In addition, the as-prepared material has a very good self-cleaning effect on the dye and dust adhering to the surface, which can greatly reduce the maintenance cost of the material. It can be easily found that the as-prepared product not only has good photocatalytic activity but also has self-cleaning performance under visible light. The results presented in this paper provide a new perspective for exploring the application of novel flexible, recyclable, and self-cleaning photocatalytic materials for environmental sustainability.

Additional file

Additional file 1: Figure S1. The optical photograph of the flexible CuS/TiO_2/PVDF fibers. **Figure S2.** The spectrum of LED white light used in the experiment. **Figure S3.** XPS survey spectrum of the CuS/TiO_2/PVDF fibers. **Figure S4.** The pseudo-first-order kinetics process of the as-prepared samples on photodegradation of RhB. **Figure S5.** Control experiments without and with radical scavengers for TiO_2/PVDF (a) and CuS/TiO_2/PVDF (b) fibers. (DOCX 1495 kb)

Abbreviations

CuS: Copper sulfide; DRS: Diffuse reflectance spectra; MB: Methyl blue; MO: Methyl orange; PL: Photoluminescence spectra; PVDF: Polyvinylidene fluoride; RhB: Rhodamine B; SEM: Scanning electron microscopy; TBOT: Tetrabutyl orthotitanate; TEM: Transmission electron microscopy; TiO_2: Titanium dioxide; XPS: X-ray photoelectron spectroscopy; XRD: X-ray diffraction

Acknowledgements

Thanks to the help of Hui Liu, Yu-Qian Cui, Min Dong, Qing-Hao Li, Xiao-Xiong Wang, Seeram Ramakrishna, and Yun-Ze Long.

Authors' Contributions

ZGZ, HL, and YZL designed the experiments. ZGZ, HL, YQC, MD, QHL, and XXW performed the experiments. ZGZ, HL, and SR analyzed the data. ZGZ and HL wrote the manuscript. YZL revised the manuscript. All authors read and approved the final manuscript.

Funding

This work was financially supported by the National Natural Science Foundation of China (51673103) and the Postdoctoral Scientific Research Foundation of Qingdao (2016014).

Availability of Data and Materials

The datasets generated during and/or analyzed during the current study are available from the corresponding authors on reasonable request.

Competing Interests

The authors declare that they have no competing interests.

Author details

[1]Collaborative Innovation Center for Nanomaterials and Devices, College of Physics, Qingdao University, Qingdao 266071, China. [2]College of Science and Information, Qingdao Agricultural University, Qingdao 266109, China. [3]College of Environmental Science and Engineering, Qingdao University, Qingdao 266071, China. [4]Center for Nanofibers and Nanotechnology, Faculty of Engineering, National University of Singapore, Singapore, Singapore.

Received: 19 February 2019 Accepted: 17 June 2019
Published online: 25 June 2019

References

1. Fujishima A, Honda K (1972) Electrochemical photolysis of water at a semiconductor electrode. Nature. 238:37–38
2. Alarawi A, Ramalingam V, Fu H, Varadhan P, Yang R, He J (2019) Enhanced photoelectrochemical hydrogen production efficiency of MoS_2-Si heterojunction. Opt Express 27:A352–A363
3. Gao W, Gou W, Zhou X, Ho J, Ma Y, Qu Y (2018) Amine-modulated/engineered interfaces of NiMo electrocatalysts for improved hydrogen evolution reaction in alkaline solutions. ACS Appl Mater Interfaces 10:1728–1733
4. Alarawi A, Ramalingam V, He J (2019) Recent advances in emerging single atom confined two-dimensional materials for water splitting applications. Materials Today Energy 11:1–23
5. Cai Z, Bu X, Wang P, Ho J, Yang J, Wang X (2019) Recent advances on layered double hydroxide electrocatalysts for oxygen evolution reaction. J Mater Chem A 7:5069–5089
6. Manikandan A, Ilango P, Chen C, Wang Y, Shih Y, Lee L, Wang Z, Ko H, Chueh Y (2018) Superior dye adsorbent towards hydrogen evolution reaction combining active sites and phase-engineering of (1T/2H) MoS_2/α-MoO_3 hybrid heterostructured nanoflowers. J Mater Chem A 6:15320–15329
7. Wei R, Fang M, Dong G, Lan C, Shu L, Zhang H, Bu X, Ho J (2018) High-index faceted porous Co_3O_4 nanosheets with oxygen vacancies for highly efficient water oxidation. ACS Appl Mater Interfaces 10:7079–7086
8. Dimitrijevic N, Tepavcevic S, Liu Y, Rajh T, Silver SC, Tiede D (2013) Nanostructured TiO_2/polypyrrole for visible light photocatalysis. J Phys Chem C 117:15540–15544
9. Dong J, Han J, Liu Y, Nakajima A, Matsushita S, Wei S, Gao W (2014) Defective black TiO_2 synthesized via anodization for visible-light photocatalysis. ACS Appl Mater Interfaces 6:1385–1388
10. Chen Q, Wu S, Xin Y (2016) Synthesis of Au-CuS-TiO_2 nanobelts photocatalyst for efficient photocatalytic degradation of antibiotic oxytetracycline. Chem Eng J 302:377–387
11. Liu H, Zhang ZG, Wang XX, Nie GD, Zhang J, Zhang SX, Cao N, Yan SY, Long YZ (2018) Highly flexible Fe_2O_3/TiO_2 composite nanofibers for photocatalysis and ultraviolet detection. J Phys Chem Solids 121:236–246
12. Zhang ZG, Wang XX, Zhang J, Yu M, Zhang JC, Zhang HD, Long YZ (2018) Recent advances in 1D micro- and nanoscale indium oxide structures. J Alloys Compd 752:359–375
13. Liu H, Zhang ZG, He HW, Wang XX, Zhang J, Zhang QQ, Tong YF, Liu HL, Ramakrishna S, Yan SY, Long YZ (2018) One-step synthesis heterostructured g-C_3N_4/TiO_2 composite for rapid degradation of pollutants in utilizing visible light. Nanomaterials. 8:842
14. Liu S, Zheng L, Yu P, Han S, Fang X (2016) Novel composites of α-Fe_2O_3 tetrakaidecahedron and graphene oxide as an effective photoelectrode with enhanced photocurrent performances. Adv Funct Mater 26:3331–3339
15. Bullock J, Amani M, Cho J, Chen Y, Ahn G, Adinolfi V, Shrestha V, Gao Y, Crozier K, Chueh Y, Javey A (2018) Polarization-resolved black phosphorus/molybdenum disulfide mid-wave infrared photodiodes with high detectivity at room temperature. Nat Photonics 12:601–607
16. Al-Amri A, Cheng B, He J (2018) Perovskite methylammonium lead trihalide heterostructures: progress and challenges. IEEE Trans Nanotechnol 18:1–12
17. Jin H, Li J, Iocozzia J, Zeng X, Wei P, Yang C, Li N, Liu Z, He J, Zhu T, Wang J, Lin Z, Wang S. Hybrid organic-inorganic thermoelectric materials and devices. 2019; doi: https://doi.org/10.1002/anie.201901106
18. Ouyang W, Teng F, He J, Fang X (2019) Enhancing the photoelectric performance of photodetectors based on metal oxide semiconductors by charge-carrier engineering. Adv Funct Mater 29:1807672
19. Liu G, Yan X, Yan F, Chen F, Hao L, Chen S, Lou T, Ning X, Long Y (2018) In situ electrospinning iodine-based fibrous meshes for antibacterial wound dressing. Nanoscale Res Lett 13:309
20. Chen S, Liu G, He H, Zhou C, Yan X, Zhang J (2019) Physical structure induced hydrophobicity analyzed from electrospinning and coating polyvinyl butyral films. Adv Cond Matter Phys 2019:6179456
21. Yan X, Yu M, Ramakrishna S, Russell S, Long Y (2019) Advances in portable electrospinning devices for in-situ delivery of personalized wound care. Nanoscale. https://doi.org/10.1039/C9NR02802A

22. Ouyang W, Teng F, Fang X (2018) High performance BiOCl nanosheets/TiO_2 nanotube arrays heterojunction UV photodetector: the influences of self-induced inner electric fields in the BiOCl nanosheets. Adv Funct Mater 28:1707178
23. Gao N, Fang X (2015) Synthesis and development of graphene-inorganic semiconductor nanocomposites. Chem Rev 115:8294–8343
24. Gordillo AH, Tzompantzi F, Omez RG' (2012) An efficient ZnS-UV photocatalysts generated in situ from ZnS $(en)_{0.5}$ hybrid during the H_2 production in methanol-water solution. Int J Hydrog Energy 37:17002–17008
25. Lee G, Kang M (2013) Physicochemical properties of core/shell structured pyrite FeS_2/anatase TiO_2 composites and their photocatalytic hydrogen production performances. Curr Appl Phys 13:1482–1489
26. Kim J, Kang M (2012) High photocatalytic hydrogen production over the band gap-tuned urchin-like Bi_2S_3-loaded TiO_2 composites system. Int J Hydrog Energy 37:8249–8256
27. Kim J, Sohn Y, Kang M (2013) New fan blade-like core-shell $Sb_2Ti_xS_y$ photocatalytic nanorod for hydrogen production from methanol/water photolysis. Int J Hydrog Energy 38:2136–2143
28. Gao P, Liu J, Zhang T, Sun DD, Ng W (2012) Hierarchical TiO_2/CdS "spindle-like" composite with high photodegradation and antibacterial capability under visible light irradiation. J Hazard Mater 229-230:209–216
29. Ratanatawanate C, Tao Y, Balkus KJ Jr (2009) Photocatalytic activity of PbS quantum dot/TiO_2 nanotube composites. J Phys Chem C 113:10755–10760
30. Shi Y, Chen Y, Tian G, Wang L, Xiao Y, Fu H (2015) Hierarchical ag/Ag_2S/CuS ternary heterostructure composite as an efficient visible-light photocatalyst. ChemCatChem. 7:1684–1690
31. Dutta S, Ray C, Mallick S, Sarkar S, Sahoo R, Negishi Y, Pal T (2015) A gel-based approach to design hierarchical CuS decorated reduced graphene oxide nanosheets for enhanced peroxidase-like activity leading to colorimetric detection of dopamine. J Phys Chem C 119:23790–23800
32. Yu S, Liu J, Zhou Y, Webster RD, Yan X (2017) Effect of synthesis method on the nanostructure and solar-driven photocatalytic properties of TiO_2-CuS composites. ACS Sustain Chem Eng 5:1347–1357
33. Lu YY, Zhang YY, Zhang J, Shi Y, Li Z, Feng ZC, Li C (2016) In situ loading of CuS nanoflowers on rutile TiO_2 surface and their improved photocatalytic performance. Appl Surf Sci 370:312–319
34. Hou G, Cheng Z, Kang L, Xu X, Zhang F, Yang H (2015) Controllable synthesis of CuS decorated TiO_2 nanofibers for enhanced photocatalysis. Crystengcomm. 17:5496–5501
35. Zhang ZG, Liu H, Zhang B, Zhang JC, Liu RZ, Ning X, Long YZ (2017) Synthesis and application of highly ordered arrays of TiO_2 rods grown on electrospun PVDF fibers. Mater Res Express 4:075907
36. Tang W, Zhu T, Zhou P, Zhao W, Wang Q, Feng G, Yuan H (2011) Poly (vinylidene fluoride)/poly (methyl methacrylate)/TiO_2 blown films: preparation and surface study. J Mater Sci 46:6656–6663
37. Mohammadi B, Yousefi AA, Bellah SM (2007) Effect of tensile strain rate and elongation on crystalline structure and piezoelectric properties of PVDF thin films. Polym Test 26:42–50
38. Yang H, Sun C, Qiao S, Zou J, Liu G, Smith SC, Cheng H, Lu G (2008) Anatase TiO_2 single crystals with a large percentage of reactive facets. Nature. 453:638–641
39. Milella E, Cosentino F, Licciulli A, Massaro C (2001) Preparation and characterisation of titania/hydroxyapatite composite coatings obtained by sol–gel process. Biomaterials. 22:1425–1431
40. Yu J, Zhao X (2001) Effect of surface treatment on the photocatalytic activity and hydrophilic property of the sol-gel derived TiO_2 thin films. Mater Res Bull 36:97–107
41. Liao S, Huang D, Yu D, Su Y, Yuan G (2004) Preparation and characterization of ZnO/TiO_2, SO_4^{2-}/ZnO/TiO_2 photocatalyst and their photocatalysis. J Photochem Photobiol A Chem 168:7–13
42. Zhang J, Yu J, Zhang Y, Li Q, Gong JR (2011) Visible light photocatalytic H_2-production activity of CuS/ZnS porous nanosheets based on photoinduced interfacial charge transfer. Nano Lett 11:4774–4779
43. Zheng L, Han S, Liu H, Yu P, Fang X (2016) Hierarchical MoS_2 nanosheet@TiO_2 nanotube array composites with enhanced photocatalytic and photocurrent performances. Small. 12:1527–1536
44. Sekiyama H, Kosugi N, Kuroda H, Ohta T (1986) Sulfur K-edge absorption spectra of Na_2SO_4, Na_2SO_3, $Na_2S_2O_3$, and $Na_2S_2O_x$ (x=5-8). Bull Chem Soc Jpn 59:575–579
45. Zhu L, Yu J, Xu Y, Xi Z, Zhu B (2009) Surface modification of PVDF porous membranes via poly (DOPA) coating and heparin immobilization. Colloids Surf, B 69:152–155
46. Zhang J, Zhao L, Long YZ, Zhang H, Sun B, Han W, Yan X, Wang X (2015) Color manipulation of intense multiluminescence from CaZnOS:Mn^{2+} by Mn^{2+} concentration effect. Chem Mater 27:7481–7489
47. Landmann M, Rauls E, Schmidt WG (2012) The electronic structure and optical response of rutile, anatase and brookite TiO_2. J Phys Condens Matter 24:195503
48. Puspitasari I, Gujar TP, Jung K, Joo O (2007) Simple chemical preparation of CuS nanowhiskers. Mater Sci Eng B 140:199–202
49. Yu C, Yang K, Shu Q, Yu JC, Cao F, Li X, Zhou X (2012) Preparation, characterization and photocatalytic performance of Mo-doped ZnO photocatalysts. Sci China Chem 55:1802–1810
50. Khanchandani S, Kumar S, Ganguli AK (2016) Comparative study of TiO_2/CuS core/shell and composite nanostructures for efficient visible light photocatalysis. ACS Sustain Chem Eng 4:1487–1499
51. AliYildirim M, Ateş A, Astam A (2009) Annealing and light effect on structural, optical and electrical properties of CuS, CuZnS and ZnS thin films grown by the SILAR method. Phys E 41:1365–1372
52. Adelifard M, Eshghi H, Mohagheghi MMB (2012) An investigation on substrate temperature and copper to sulphur molar ratios on optical and electrical properties of nanostructural CuS thin films prepared by spray pyrolysis method. Appl Surf Sci 258:5733–5738
53. Yuan Y, Ye Z, Lu H, Hu B, Li Y, Chen D, Zhong J, Yu Z, Zou Z (2016) Constructing anatase TiO_2 nanosheets with exposed (001) facets/layered MoS_2 two-dimensional nanojunctions for enhanced solar hydrogen generation. ACS Catal 6:532–541
54. He H, Lin J, Fu W, Wang X, Wang H, Zeng Q, Gu Q, Li Y, Yan C, Tay BK, Xue C, Hu X, Pantelides ST, Zhou W, Liu Z (2016) MoS_2/TiO_2 edge-on heterostructure for efficient photocatalytic hydrogen evolution. Adv Energy Mater:1600464
55. Liu B, Wen L, Zhao X (2007) The photoluminescence spectroscopic study of anatase TiO_2 prepared by magnetron sputtering. Mater Chem Phys 106:350–353
56. Karunakaran C, Abiramasundari G, Gomathisankar P, Manikandan G, Anandi V (2010) Cu-doped TiO_2 nanoparticles for photocatalytic disinfection of bacteria under visible light. J Colloid Interface Sci 352:68–74
57. Abazović ND, Čomor MI, Dramićanin MD, Jovanović DJ, Ahrenkiel SP, Nedeljković JM (2006) Photoluminescence of anatase and rutile TiO_2 particles. J Phys Chem B 110:25366–25370
58. Yang Y, Wen J, Wei J, Xiong R, Shi J, Pan C (2013) Polypyrrole-decorated ag-TiO_2 nanofibers exhibiting enhanced photocatalytic activity under visible-light illumination. ACS Appl Mater Interfaces 5:6201–6207
59. Tan C, Zhu G, Hojamberdiev M, Okada K, Liang J, Luo X, Liu P, Liu Y (2014) Co_3O_4 nanoparticles-loaded BiOCl nanoplates with the dominant {001} facets: efficient photodegradation of organic dyes under visible light. Appl Catal B Environ 152(153):425–436
60. Teng W, Wang Y, Huang H, Li X, Tang Y (2017) Enhanced photoelectrochemical performance of MoS_2 nanobelts-loaded TiO_2 nanotube arrays by photo-assisted electrodeposition. Appl Surf Sci 425:507–517

Publisher's Note